Received: November 18, 2020
Revised: December 27, 2020
Accepted: December 28, 2020

Manganese Oxide Carbon Nanocomposite from Manganese Oxide Nanoparticles and Cellulose Carbonization for electrochemical energy storage applications

Weerachon Phoohinkong * and Thitinat Sukonket

Faculty of Science and Technology, Suan Dusit University, Bangkok, 10700, Thailand

Abstract

The synthesis of manganese oxide embedded carbon nanocomposite by direct carbonization of nano-sized manganese oxide/cellulose hybrid nanocomposite is reported. X-ray diffraction (XRD) and X-ray photoelectron spectroscopy (XPS) were used to characterize surface phase structure and chemical states. Field emission scanning electron microscope (FESEM) and transmission electron microscope (TEM) were used to study its particle size, structure, and composite morphology. Cyclic voltammetry (CV) was used to study the electrochemical capacitor activity of the electro-active sample. Manganese oxide cellulose hybrid nanocomposite exhibits the existence of manganese oxide nanoparticles (≈50 nm) that are well assembled and homogeneously dispersed in carbon after the carbonization process. The mixed-valence states of Mn_3O_4 hausmannite with different Mn ionic species of Mn^{2+}, $Mn^{3+,}$ and Mn^{4+} were obtained at the carbonized surface sample. The improvement of electrochemical performance of the prepared manganese oxide carbon nanocomposite sample may attribute to various oxidation levels, and increased conductivity via strong bonding between manganese oxide and carbon leading to feasibility for application of supercapacitor electrode material.

Keywords: Manganese oxide, multivalence, Carbon, Cellulose, Nanocomposite

1. Introduction

Manganese oxide is one of the most important electroactive materials for supercapacitor electrodes, widely studied for energy storage devices due to its low cost, long-life cycling, large window potential. Moreover, manganese oxide has high capacitance and power density property via both pseudo capacitances by Faradaic redox mechanism and electrical double layer mechanism [1-6]. Various synthesis methods have been investigated for supercapacitor application such as annealing of manganese salt [1], chemical bath deposition [3], hydrothermal routes [2], and electrodeposition [5], et cetera. To improve a superior electrochemical capacitance performance, enhancing the specific surface area and electronic conductivity was necessary. To solve these problems, carbon nanostructure materials coupling with nano-sized manganese oxide have been widely investigated due to high electric conductivity, chemical stability, abundant and large specific surface area [7,8]. Different carbon materials including activated carbon [7,9], carbon fabric [8], carbon nanotube [10], graphene, and graphene oxide [11-15] also have been interesting research for composite with manganese oxide [7-15] via different synthesis method such as precipitation [9] and hydrothermal process [8, 10-12], which have been reported that improve specific capacitance.

Cellulose is one of the most important carbon sources for use as metal oxide carbon nanocomposite due to cheap, abundant from renewable biomass, and easy to use for synthesis carbon-metal oxide nanocomposite. Therefore, increasing attention in the study on preparation

Corresponding Author E-mail: p_veerachon@hotmail.com

and characterization of manganese oxide carbon nanocomposite from cellulose-based [16-19]. In this work, we synthesis Mn_3O_4 hausmannite embedded carbon nanocomposite using nanocellulose as binder and carbon source via direct carbonization method for increase conductivity, stabilize nanoMn_3O_4 particle, and prevent agglomeration during potential cycling. The prepared sample presents multivalence Mn species at the surface and clearly shows higher capacitance than that the starting manganese oxide nanoparticle. This method also simple, low cost and scale up able remarkable promising for supercapacitor technology.

2. Experimental details

2.1. Synthesis of manganese oxide nanoparticle embedded carbon nanocomposite

The starting manganese oxide nanoparticle in Mn_3O_4 hausmannite structure was synthesized by simple solid-state reaction method as ascribe in our previous work [20] briefly, grinding the mixture of manganese sulfate ($MnSO_4$ H_2O) salt and NaOH in a mortar at room temperature for 20 min. Wash the resulting with DI water several times. Dried the resulting solid residual at 80 ^oC for 24h. The starting Mn_3O_4 nanoparticle is denoted as n-Mn_3O_4.

The nanocellulose was prepared from sugarcane bagasse using acid hydrolysis followed by the ball milling method [21, 22]. Firstly, the bagasse was washed with DI water several times, after drying overnight the precision weight were treated with ethanol. Secondly, bleach the sugarcane bagasse fiber in 4% NaOH 24% H_2O_2 aqueous solution at 60 ^oC for 2h. Finally, the bleached cellulose fiber was mixed with 5 and 2 mm diameter size of zirconia ball and milling at 225 rpm for 12h. The milled cellulose was then hydrolysis with 50% H_2SO_4 and washed with DI water until neutralized pH was obtained. Mix the nanocellulose and Mn_3O_4 nanoparticle at 2:8 wt% in aqueous. The dry mixture of cellulose and Mn_3O_4 nanocomposite at 50 ^oC for 24h was denoted as C-$Mn_3O_4$50. The carbonization of C-$Mn_3O_4$50 nanocomposite was conducted at 500 ^oC in a muffle furnace for 2h to obtain a dark brown powder sample of manganese oxide carbon nanocomposite and named C-$Mn_3O_4$500. For the comparison study, the n-Mn_3O_4 also anneal at the same condition named $Mn_3O_4$500.

2.2. Characterization and Electrochemical Tests

XRD measurements were performed by a Rigaku diffractometer (Dmax-2200) using Cu Kα radiation. The diffraction spectra were collected from 5 to 80^o. X-ray absorption spectroscopic (XAS) at beamline 8 station (BL8) of the Synchrotron Light Research Institute (SLRI) were used to characterize the samples, pure Mn metal foil, and reference materials by mean of X-ray absorption near-edge spectra (XANES) at the Mn K-edge region in transmission mode. Data subtraction and processing by the ATHENA software. Particle morphology was observed by field emission scanning electron microscope (FESEM) HITACHI-S47000. FTIR data were carried out by FTRI IRTracer-100 Shimadzu. Binding energy spectra were investigated by XPS AXIS Ultra DLD, Kratos Analytical, Shimadzu. Electrochemical cyclic voltammetry was tested in 1.0 M Na_2SO_4 electrolyte with Ag/AgCl reference electrode. The electro-active samples of 3 mg were placed on 4 X 5 mm^2 carbon planar electrodes without any binder or additive. The CV profile collects by Autolab PGSTAT302N and NOVA 2.1 software.

3. Results and discussion

As-synthesized manganese oxide nanoparticles (n-Mn_3O_4) and manganese oxide nanoparticle embedded carbon nanocomposite (C-$Mn_3O_4$500) X-ray diffraction patterns show in Fig. 1. The main diffraction pattern of the n-Mn_3O_4 corresponds to the spinel-type Mn_3O_4 hausmannite with JCPDS 01 0800382 and 00 240734 belongs to the distorted tetragonal group which Mn^{2+} state in the tetrahedral site and Mn^{3+} state in the octahedral site [1-3]. The secondary X-ray diffraction patterns found in the starting material n-Mn_3O_4 corresponds to the JCPDS 411379 database of γ-MnO(OH) manganite phase, which manganese occupy in Mn^{3+} state.

The prepared C-$Mn_3O_4$500 sample presents the main diffraction peak at 18.0°, 29.0°, 31.0°, 32.4°, 36.1°, 38.2°, 44.4°, 50.9°, 58.6°, 60.0°, 64.7°, and 74.3° correspond to (101), (112), (200), (103), (211), (004), (220), (105), (321), (224), (400) and (413) planes belong the same pattern of Mn_3O_4 hausmannite in the starting manganese oxide nanoparticles. The minor phase shows characteristic peaks index to Mn_2O_3 at 23.2°, 33.0°, 55.1°, and 65.8° correspond to (221), (222), (440), and (662) planes, respectively. To explicitly distinguish peaks, the overlay XRD patterns depict at the top of Fig. 1. The overlapped peaks (dark green) indicated the main phase with the same pattern of Mn_3O_4 hausmannite in both samples. The residual peaks (red) of the n-Mn_3O_4 sample refer to γ-MnO(OH) manganite and the lite green peaks of the C-$Mn_3O_4$500 sample correspond to the pattern of Mn_2O_3 structure.

There are no crystal peak patterns or amorphous characteristics of the carbon phase in the prepared sample which typical domain (002) plane reflex Bragg's angle around 25-26°. The low graphitization degree of carbon due to nanocomposite with Mn_3O_4 [23] and/or the low carbonization degree of cellulose. The existence of γ-MnO(OH) manganite may support the formation of Mn_3O_4 hausmannite via a solid-state reaction mechanism through MnO(OH). The remaining MnO(OH) attribute to the high ratio of NaOH reactance resulting react with Mn_3O_4 facilitates MnO(OH) phase [24] and insufficient oxygen due to strong fast reaction in the solid-state reaction.

XANE spectra of manganese oxide reference material and samples were recorded at Mn K-edge reflex pattern of bulk local structure around Mn atom as Mn_3O_4 structure for all samples were shown in Fig. 2. [25-28]. The edge energy rising due to 1*s* to the continuum transition absorption and the Mn pre-K-edge due to 1*s* to 3*d* and 4*p* hybridized transition absorption was shown in (a) and (b) inset plot (Fig. 2.), respectively. The result reveals that local symmetry environs around Mn atom and oxidation state corresponding to Mn_3O_4 hausmannite structure for all sample [26,29]. The C-$Mn_3O_4$500 and starting n-Mn_3O_4 samples show the same pattern of Mn_3O_4 spectra except for lower oscillation intensity in the C-$Mn_3O_4$500 due to lower crystallinity in bulk. The C-$Mn_3O_4$500 pre-K-edge shape spectra and edge energy ware identical to the starting n-Mn_3O_4 and C-$Mn_3O_4$50 reveal that the manganese oxide phase can be stabilized by nanocellulose during the anneal step.

FESEM image in Fig. 3a demonstrates that a nodular round in diameter size less than 30 nm of the n-Mn_3O_4 sample. Fig. 3b shows the perspective picture of C-$Mn_3O_4$500 sample agglomerate in large irregular morphology particle within the different size, while the high magnitude reveals that manganese oxide present at surface particle Fig. 3c and manganese oxide embedded in carbon metric Fig. 3d. A small part of manganese at the surface indicated crystal growth to a larger size in octahedral and truncated octahedron shape were observed. Most of the starting Mn_3O_4 nanoparticles (n-Mn_3O_4 sample) were well dispersed embedded in carbon and also indicated a nodular round shape with diameter size in the range of 50-80 nm.

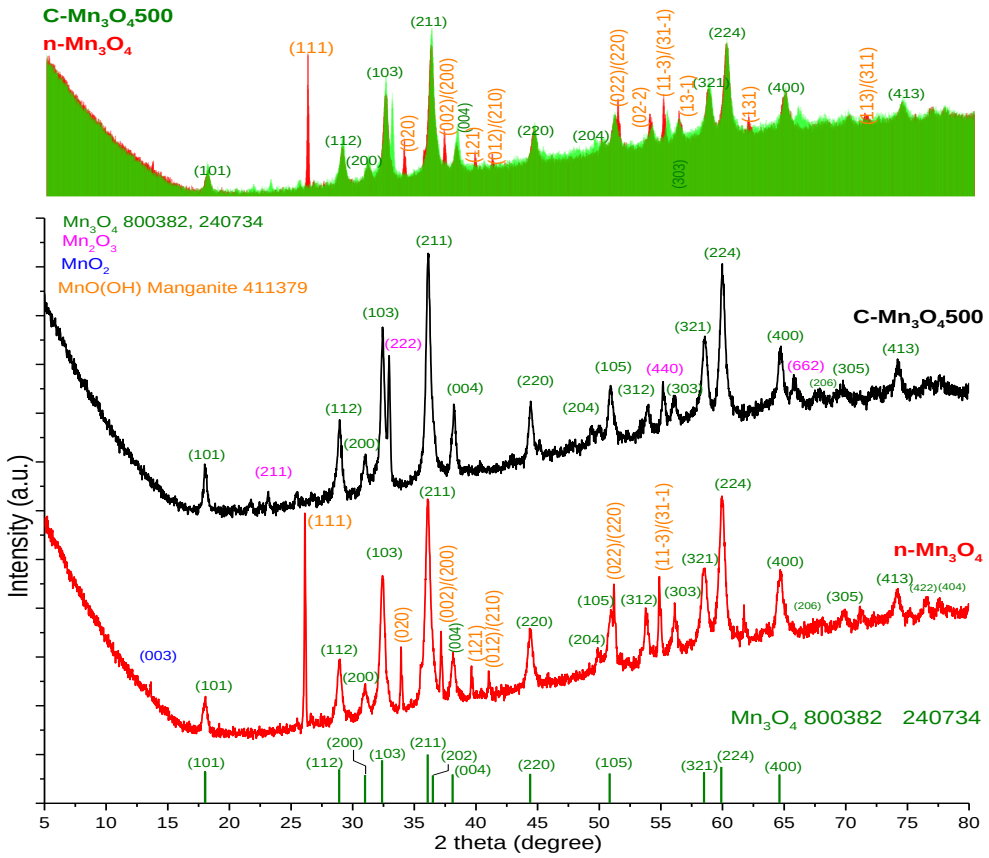

Fig. 1. XRD patterns of the n-Mn_3O_4 and C-$Mn_3O_4$500 samples with JCPDS 800382, 240734 spectrums.

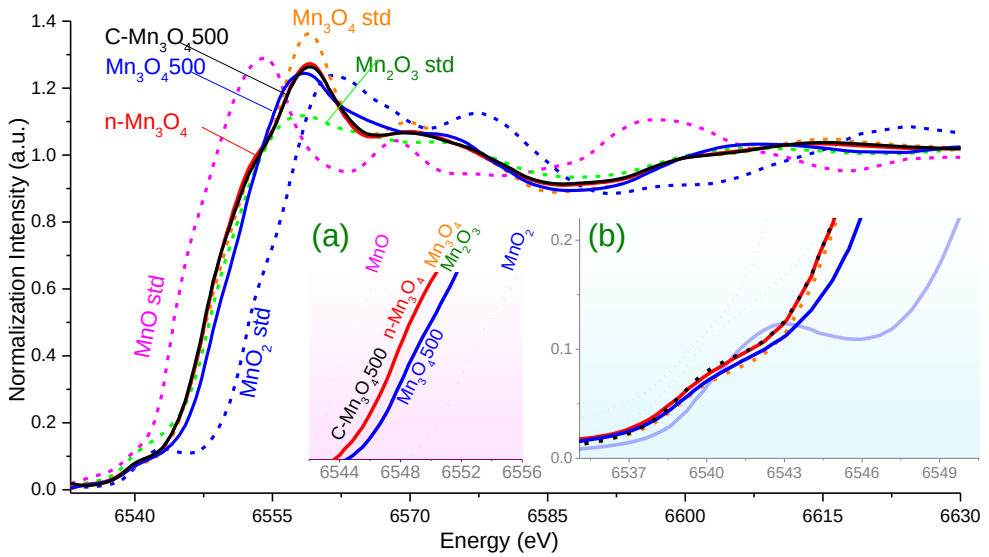

Fig. 2. Mn K-edge XANES spectra of n-Mn_3O_4, $Mn_3O_4$500, and C-$Mn_3O_4$500 samples compared with standard materials.

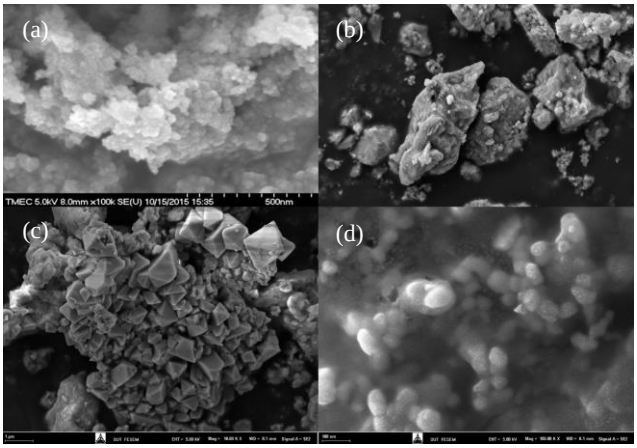

Fig. 3. FESEM image of the n-Mn_3O_4 (a), C-$Mn_3O_4$500 sample for 10k at large irregular morphology particle area (b), the region of surface manganese oxide (c), and for 100k at the surface of manganese oxide embedded in carbon metric (d).

The result of FTIR analysis in Fig. 4b shows typical spectra of n-Mn_3O_4, $Mn_3O_4$500, cellulose modify with n-Mn_3O_4 after heat treatment at 50 ºC (C-$Mn_3O_4$50) step and the final carbonized C-$Mn_3O_4$500 samples, indicated a major band of metal oxide vibration which clear in the enlargement at Fig. 4c. The main adsorption band at wave number around 500 to 700 cm^{-1} corresponding to Mn-O vibration in the lattice which deconvolutes for more information shows in Fig. 4b. Mn-O stretching in Mn_3O_4 lattice for tetrahedral and octahedral symmetry energy are in the peak at around 603 and 529 cm^{-1}, respectively [30-33]. The peak at 858 cm^{-1} evidence that manganite MnOOH phase composition in C-$Mn_3O_4$500 sample corresponding to Mn-O stretching mode. The strong evidence of manganite MnOOH phase composition confirmed by characteristic band pattern of O-H stretching around 2600 to 1700 and at 2060 cm^{-1}, as depicted in the inset Fig 4a [31-34]. Fig. 4c in the n-Mn_3O_4 sample clearly shows the fingerprint peak of OH in manganite lattice vibration corresponding to δ-1-OH, δ-2-OH, and out-of-plane γ–OH bending mode at 1146, 1115 and 1087 cm^{-1}, respectively [31-34]. XRD and FTIR results confirmed manganite MnOOH diminish in the C-Mn_3O_4 sample.

The peak at 559 and 661 cm^{-1} in the n-Mn_3O_4 sample (Fig. 4b) were assigned to TO and LO mode of Mn-O vibration of Mn_2O_3 confirmed that the composition of the Mn_2O_3 phase in the n-Mn_3O_4 sample, agree with the XRD result. Vibration energy peaks at around 596 - 603 and 528 cm^{-1} correspond to Mn-O stretching mode for tetrahedral and octahedral coordination of Mn_3O_4 lattice which present in n-Mn_3O_4, C-$Mn_3O_4$50 and C-$Mn_3O_4$500 samples. The peak composition in this region indicated that nanocellulose can stabilize the Mn_3O_4 hausmannite phase compare with $Mn_3O_4$500 may be due to prevent the reaction from exceeded oxygen.

IR band in OH bending region of C-$Mn_3O_4$50 (Fig. 4c) indicated broad shape due to overlap with C-O-C peak component which typical C-O-C asymmetric in-phase ring stretching mode in pyranose ring of cellulose present band around 1025 – 1161 cm^{-1} confirm with C-O-C of glycosidic linkage between glucose unit in cellulose at 827 cm^{-1} [20,21,35]. In general, nanocellulose structure unstable at over 50 ºC. The IR characteristic of β-glycosidic linkage in cellulose comprises glycosidic C-H deformation vibration mode contribute with O-H bending mode at the wavenumber around 897-902 cm^{-1}. This IR region shows weak and broad at slightly higher energy than the C-H characteristic. The C-OH stretching peak in

the pyranose ring of cellulose at around 1028 cm^{-1} shifts to higher energy at 1019 cm^{-1}. These results imply that nanocellulose strong bonding to the n-Mn_3O_4 surface of the C-$Mn_3O_4$50 sample. There is no characteristic of cellulose IR spectra confirmed that cellulose was completely carbonized to carbon.

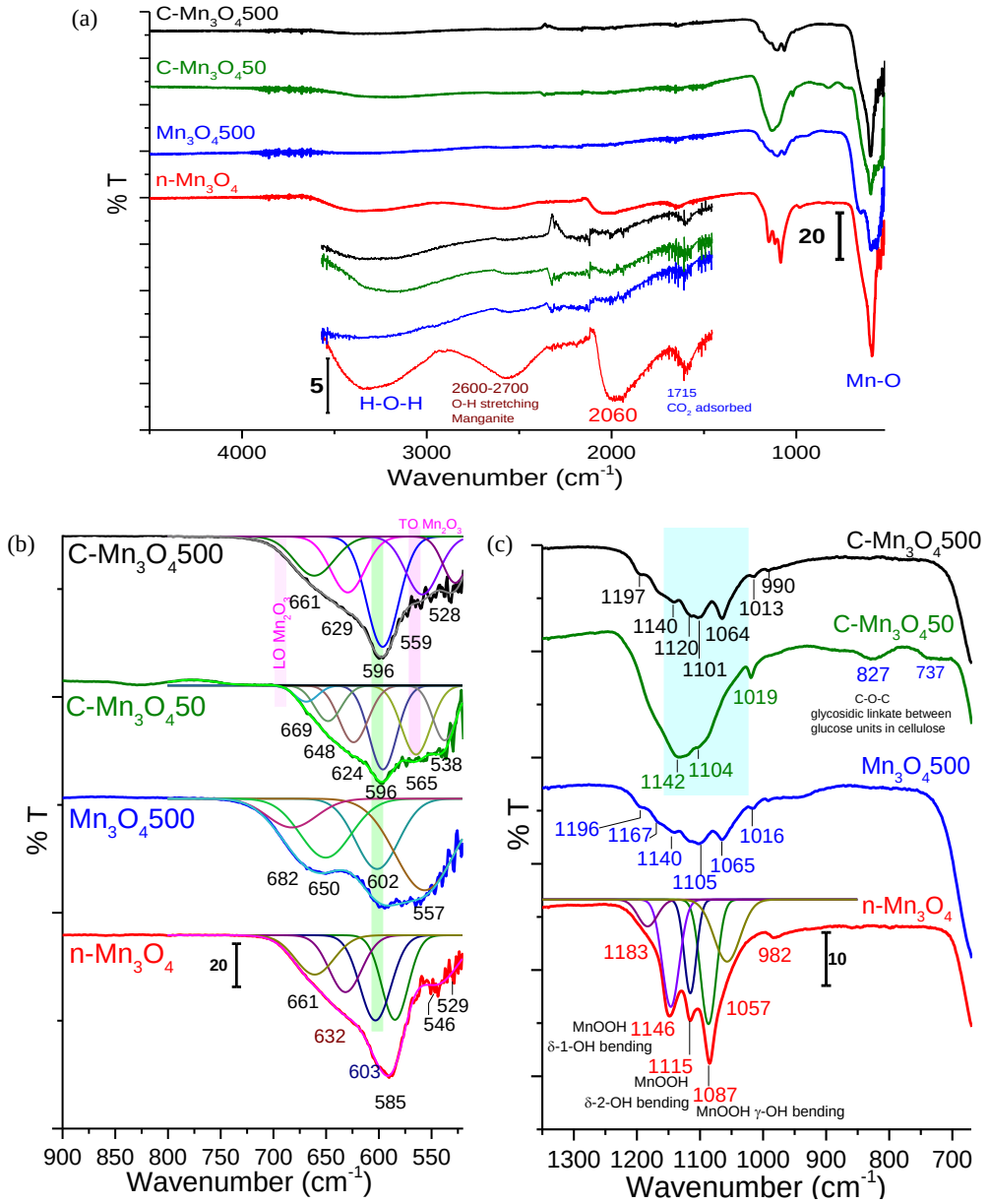

Fig. 4. Fourier-transform infrared spectra of the n-Mn_3O_4, $Mn_3O_4$500, C-$Mn_3O_4$50, and C-$Mn_3O_4$500 samples (a). The expanded-view of the samples present in the region of Mm-O vibration in the lattice (b), and the region of MOOH and cellulose C-O-C pyranose ring characteristic (c). The green bar indicated the region of hausmanite Mn_3O_4 peak characteristic, the magenta bar at a wavenumber of around 691 and 565 cm^{-1} assigned to LO and TO vibration mode, and the light-blue bar for the region of C-O-C pyranose ring and C-OH stretching characteristic of cellulose.

The electronic structure was investigated for the n-Mn_3O_4, $Mn_3O_4$500, and C-$Mn_3O_4$500 samples. The XPS survey scan analysis carried out in the range of binding energy between 0 to 1200 eV were show in Fig. 3a, indicated the main composition of Mn*2p*, O*1s*, C*1s* correspond to valence peaks of Mn*3p* and Mn*3s* [36-39]. The surface impurities significant present at binding energy around 168 eV for all samples correspond to S*2p* which due to the surface adsorbed sulfate product [40,41]. The C*1s* peak of the C-$Mn_3O_4$500 sample shows distinguished highly peak intensity indicated that high carbon content derived from cellulose.

The high-resolution XPS spectra of the sample at C*1s*, O*1s*, and Mn*2p* core levels were present in Fig. 5b-d, respectively. The C*1s* peak fitting corresponds to the carbon chemical state which relates to the carbon atom in the different functional groups. The peak at binding energy 284.7 eV corresponds to C-C, C=C, C-H of amorphous carbon atom as standard binding energy. The carbon impurity adsorbed on starting n-Mn_3O_4 also contains the peaks at 286.3, 287.9, and 289.1 eV attribute to –C-OH, >C=O, and –COOR, respectively. The $Mn_3O_4$500 C*1s* show the addition of peak at 287.0 and 291.0 eV attributed to C-O-C and π-π* shake-up satellite of graphitic carbon without the –COOR signal indicated that all adsorbed carbon impurity was completely carbonized to carbon in this annealing condition [42-44]. The peaks at 285.9, 288.4, especially 287.2 eV increasing intensity in the C-$Mn_3O_4$500 sample corresponding to C-OH, C=O/O-C-O, and epoxide/C-O-C bonding from cellulose. The C*1s* C=O binding energy peak at 288.4 eV of $Mn_3O_4$500 may be attributed to contributing with main acetal O-C-O bonding in melt cellulose and the high-intensity peak of 287.2 eV due to glycosidic linkage C-O-C in melt cellulose [45-47].

Hydroxyl, carbonyl, and carboxyl groups should be used to cross-link the site at the interface by C-O-Mn bonding linkage [37, 48]. However, the high-intensity in this peak (287.2 eV) consists of the combination of the cellulose hydroxyl interlink, C-O-C, and O-C-O components. The appearance of C=O and COOH groups typical due to cellulose unit decomposition product during cellulose pyrolysis and may include with epoxide group [49,50]. Moreover, graphitic carbon also occurs correspond to π-π* peak at 291.1 eV indicated that partial cellulose carbonizes to carbon aromatic structure composite with amorphous melt cellulose structure at surface particle agree well with XRD and FTIR results.

The O*1s* fine scan spectra (Fig. 5c) of the n-Mn_3O_4 sample show two main peaks at 530.1 eV and a smaller peak at 531.3 eV was attributed to Mn-O-Mn in the lattice of Mn_3O_4 and Mn-OH in MnO(OH) phase, respectively [37, 38, 42, 51-53]. The binding energy peaks at 532.3, 533.4, and 534.4 eV were assigned to adsorbed C=O, O-H/H_2O, and COOH, respectively [37, 38, 51]. The Mn-O-Mn (529.9-530.3 eV) and Mn-OH (531.0-531.3 eV) peaks intensity decrease in order of n-Mn_3O_4, $Mn_3O_4$500, and C-$Mn_3O_4$500 indicated that, manganese hydroxide decomposition to manganese oxide at 500 ^oC. The Mn-OH bonding for C-Mn_3O_4 was also stated that of O-C-OH and a small part of Mn-OC cross-link [37], since the MnO(OH) phase was depleted account to binding energy shift at 531.0 eV. C=O bonding intensity of C-Mn_3O_4 lower than impurity of $Mn_3O_4$500 may evidence that Mn-OC cross-link occurs via C=O group. High COOH peak at around 534.3 eV due to carbon from cellulose, interesting that, high chemisorbed oxygen at 535.6 eV was obtained [43,54].

Mn*2p* XPS spectra of the samples show large spin-orbit by deconvoluting analysis in the region of Mn$2p_{3/2}$ in Fig. 5d. Typical 2*p* XPS spectra were complex by multiplet splitting, shake-up, plasmon loss, and overlap of binding energy [55]. Since the samples are mixed-phase including multivalence Mn^{2+}/Mn^{3+} of hausmannite and Mn^{3+} of manganite which Mn_2O_3 and MnO_2 probably count at the samples surfaces, various crystal field effect due to

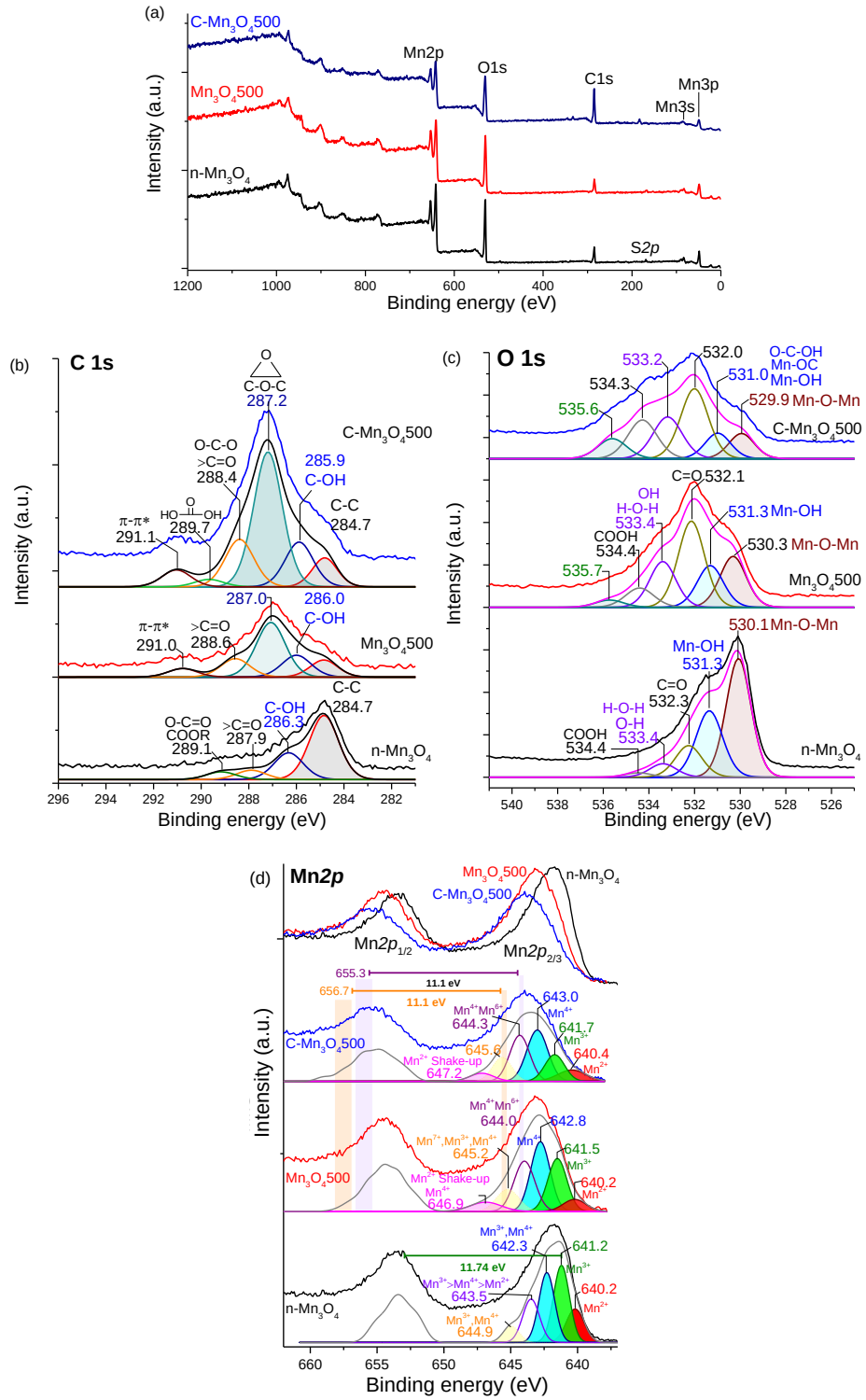

Fig. 5. XPS spectra of the n-Mn_3O_4, $Mn_3O_4$500, and C-Mn_3O_4 samples for survey scan (a), and core level fine scan at C*1s* (b), O*1s* (c), and Mn*2p* (d).

different local symmetry around Mn atom which tetrahedral and octahedral symmetry in hausmannite phase and distort octahedral symmetry in other phases also may contribute with surface defect [56-58]. To achieve the best fitting with the experiment curve for detailed reliable accurate relative oxidation state information, the binding energy peak component was carefully deconvoluted with the narrowest FWHM close to 1.0 eV after Shirley background subtraction. The multiplet splitting fitting spectra of Nesbitt and Banerjee [59] from the theoretical calculations based by Gupta and Sen [60,61] supplement with multicomponent fitting spectra of standard material from references [55, 62-65] were used to achieve an accurate interpretation binding state. The fitted Mn$2p_{3/2}$ of the n-Mn_3O_4 sample having 5 component binding energy peaks at 640.2, 641.2, 642.3, 643.5, and 644.9 eV. The binding energy peaks at 640.2 (red) and 641.2 eV (green) correspond to the main populations of Mn^{2+} and Mn^{3+} states, respectively. The peak at 642.3 eV (blue) correlates to the subordinate peak of Mn^{3+} state contribute to the small composition of Mn^{4+} state from MnO_2 composition since the small MnO_2 presented in XRD result. The binding energy peak at 643.5 eV corresponds to the combination of Mn^{3+}, Mn^{4+} and Mn^{2+} subordinate state of hausmannite and manganite while the peak at 644.9 eV relative to contribution from Mn^{3+} and Mn^{4+} multiplet component. The Mn*2p* component spectra of $Mn_3O_4$500 show a peak of 642.8 eV (Mn^{4+}) intensity increase while the peak at 641.5 eV (Mn^{3+}) intensity decrease from n-Mn_3O_4 ascribes to increase of Mn^{4+} content. The peak intensity ratio of Mn^{3+} (green) to Mn^{4+} (blue) was decreased in the order of the n-Mn_3O_4, $Mn_3O_4$500, and C-$Mn_3O_4$500 samples ascribe to increase of Mn^{4+} content while the Mn^{3+} content decrease. The binding energy peak at around 644 eV (violet) corresponds to the combination of Mn^{3+}, Mn^{4+}, and Mn^{2+} state components and the peak at around 645 eV (yellow) corresponds to the combination of Mn^{3+}, and Mn^{4+} state components for the n-Mn_3O_4. The peaks at around 644 eV (violet) of the $Mn_3O_4$500 and C-$Mn_3O_4$500 sample corresponds to the combination of Mn^{4+} and Mn^{6+} state components. The yellow peak of the $Mn_3O_4$500 and C-$Mn_3O_4$500 sample corresponds to the combination of Mn^{7+}, Mn^{3+}, and Mn^{4+} state components. The combination of Mn^{6+} and Mn^{7+} component in the violet and yellow peaks of the $Mn_3O_4$500 and C-$Mn_3O_4$500 sample were confirmed by Mn$2p_{1/2}$ band located around 655.3 and 656.7 eV, respectively with the 11.1 eV spin-orbit splitting fingerprint characteristic [36, 55, 66, 67]. The peak at 646.9 eV is major due to the shake-up peak of Mn^{2+} associated with a tiny component state of Mn^{4+}. C-Mn_3O_4 sample, the fitted 5 component binding energy peaks were obtained correspond to of n-Mn_3O_4 component with slight energy shift but lower peak intensity evidence due to carbon-coated at the surface and multi-state of multi coordination bonding environment with Mn-O-C interface linkage. The highly Mn oxidation state on the surface Mn^{6+} and Mn^{7+} state component increases since the ratio of Mn^{4+} and Mn^{3+} major component peak to Mn^{6+} and Mn^{7+} peaks decrease. The mixed of multivalency lead to enhanced charge transfer and conductivity between manganese and carbon.

The cyclic voltammogram of different scan rates for 5, 10, 50, and 100 mV/s of the n-Mn_3O_4 and C-$Mn_3O_4$500 sample is shown in Fig. 6a and b, respectively. The high current density with capacitor behavior of rectangular CV shape of the n-Mn_3O_4 sample was obtained imply that due to low diffusion distance and high active surface area of nanoparticle and probably synergistic effect of MnOOH phase [1, 39, 56, 68]. However, the C-$Mn_3O_4$500 sample shown superior current density compare with the n-Mn_3O_4 sample as present at a scan rate of 100 mV/s (Fig. 6c). The CV shape of the C-$Mn_3O_4$500 sample is shown both electrochemical double-layer capacitor behavior and pseudocapacitor behavior. The Faradaic current may rise due to the active surface site of an octahedral and truncated octahedron of Mn_3O_4 {111} exposed [2].

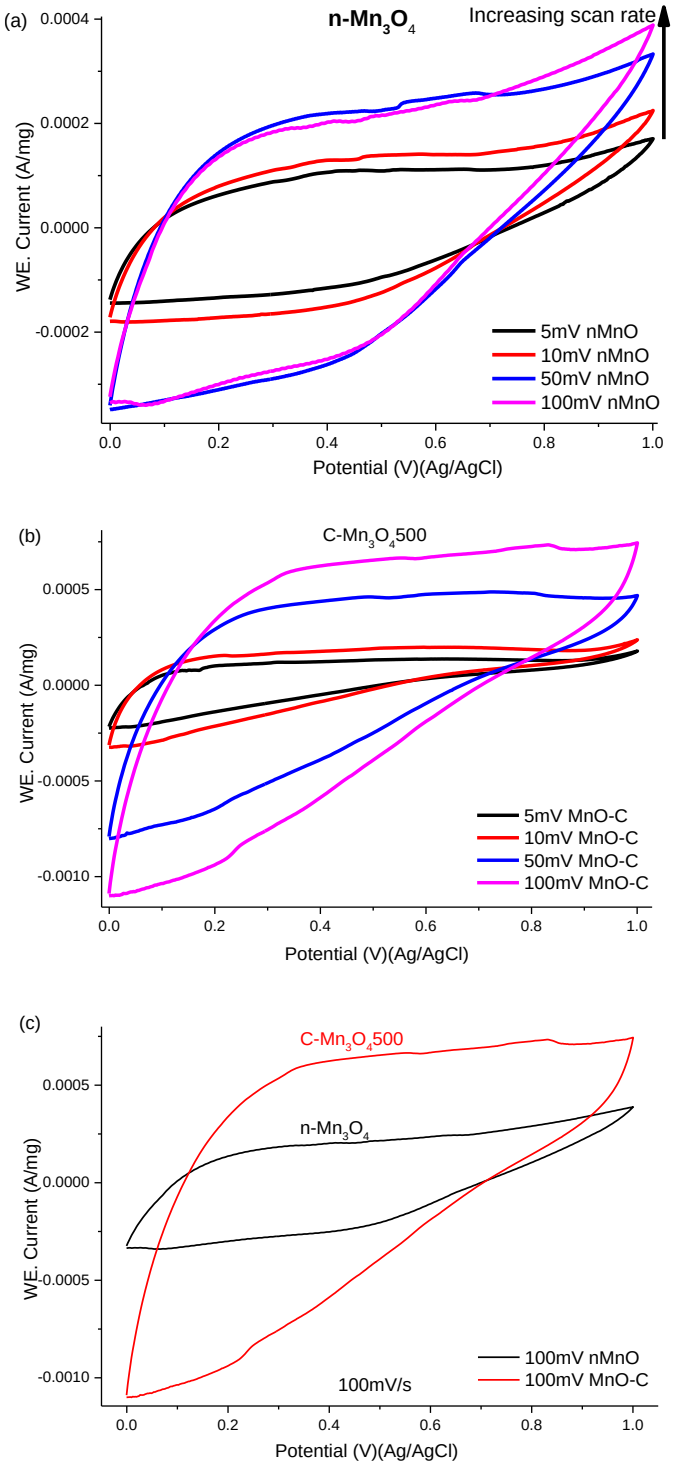

Fig. 6. CV curve of (a) n-Mn_3O_4, (b) C-$Mn_3O_4$500, and compared two samples at a sweep rate of 100 mVs^{-1} vs Ag/AgCl in 1.0 M Na_2SO_4 (c).

4. Conclusion

The starting manganese oxide nanoparticle consists of amorphous Mn_3O_4 and hausmannite Mn_3O_4 as the main phase with the minor phase of manganite MnOOH nanoparticle. The starting manganese oxide nanoparticle showed high capacitance due to the large surface area and the synergistic effect of mixed phase. Nanocellulose has been shown advance for use as a binder and carbon source for the synthesis of electroactive manganese oxide electrode nanohybrid material. The manganese oxide carbon nanocomposite in this work demonstrated better both electric double layer and pseudocapacitive performance than bare manganese oxide nanoparticles. The superior capacitive performance is attributed to the improvement of surface morphology, active surface area, multivalence surface state, particle size, morphology structure, and interface connectivity between manganese oxide and carbon by using cellulose as a carbon source. The use of nano-cellulose precursors can control phase and particle structure growth as well as create surface multi-state Mn components which remarkable promising advance for supercapacitor electrode technology.

Acknowledgment

We gratefully thank the beamline 8 (BL8) Synchrotron Light Research Institute (Public Organization) for XAS experiments.

References

[1] Wu T-H, Hesp D, Dhanak V, Collins C, Braga F, Hardwick LJ, et al. Charge storage mechanism of activated manganese oxide composites for pseudocapacitors. J. Mater. Chem. A 2015;3:12786-95.

[2] Jiang H, Zhao T, Yan C, Ma J, Li C. Hydrothermal synthesis of novel Mn_3O_4 nano-octahedrons with enhanced supercapacitors performances. Nanoscale. 2010;2:2195-8.

[3] Dubal DP, Dhawale DS, Salunkhe RR, Pawar SM, Fulari VJ, Lokhande CD. A novel chemical synthesis of interlocked cubes of hausmannite Mn_3O_4 thin films for supercapacitor application. J. Alloys Compd. 2009;484:218-21.

[4] Dubal DP, Jagadale AD, Lokhande CD. Big as well as light weight portable, Mn_3O_4 based symmetric supercapacitive devices: Fabrication, performance evaluation and demonstration. Electrochim. Acta 2012;80:160-70.

[5] Yousefi T, Golikand A, Mashhadizadeh MH, Aghazadeh M. High temperature and low current density synthesis of Mn_3O_4 porous nano spheres: Characterization and electrochemical properties. Curr. Appl Phys. 2012;12:544-9.

[6] Luo Y, Yang T, Li Z, Xiao B, Zhang M. High performance of Mn_3O_4 cubes for supercapacitor applications. Mater. Lett. 2016;178:171-4.

[7] Makgopa K, Raju K, Ejikeme PM, Ozoemena KI. High-performance Mn_3O_4/onion-like carbon (OLC) nanohybrid pseudocapacitor: Unravelling the intrinsic properties of OLC against other carbon supports. Carbon 2017;117:20-32.

[8] Ullah Shah H, Wang F, Sufyan Javed M, Shaheen N, Ali S, Ashfaq Ahmad M, et al. Mn_3O_4 nanosheets decorated on flexible carbon fabric for high-performance supercapacitors electrode. Mater. Lett. 2018;210:148-52.

[9] Bùi MP, Song J-H, Li Z-Y, Akhtar MS, Yang OB. Low temperature solution processed Mn_3O_4 nanoparticles: Enhanced performance of electrochemical supercapacitors. J. Alloys Compd. 2016;694:560-7.

[10] Mondal C, Ghosh D, Aditya T, Sasmal AK, Pal T. Mn_3O_4 nanoparticles anchored to multiwall carbon nanotubes: a distinctive synergism for high-performance supercapacitors. New J. Chem. 2015;39:8373-80.
[11] Wu Y, Liu S, Wang H, Wang X, Zhang X, Jin G. A novel solvothermal synthesis of Mn_3O_4/graphene composites for supercapacitors. Electrochim. Acta 2013;90:210-8.
[12] Yao J, Yao S, Gao F, Duan L, Niu M, Liu J. Reduced graphene oxide/Mn_3O_4 nanohybrid for high-rate pseduocapacitive electrodes. J. Colloid Interface Sci. 2018;511:434-9.
[13] Wang L, Li Y, Han Z, Chen L, Qian B, Jiang X, et al. Composite structure and properties of Mn_3O_4/graphene oxide and Mn_3O_4/graphene. J. Mater. Chem. A 2013;1:8385-97.
[14] Gund GS, Dubal DP, Patil BH, Shinde SS, Lokhande CD. Enhanced activity of chemically synthesized hybrid graphene oxide/Mn_3O_4 composite for high performance supercapacitors. Electrochim. Acta 2013;92:205-15.
[15] Wang B, Park J, Wang C, Ahn H, Wang G. Mn_3O_4 nanoparticles embedded into graphene nanosheets: Preparation, characterization, and electrochemical properties for supercapacitors. Electrochim. Acta 2010;55:6812-7.
[16] He S, Hu C, Hou H, Chen W. Ultrathin MnO_2 nanosheets supported on cellulose based carbon papers for high-power supercapacitors. J. Power Sources 2014;246:754-61.
[17] Ma M-G, Deng F, Yao K. Manganese-containing cellulose nanocomposites: The restrain effect of cellulose treated with NaOH/urea aqueous solutions. Carbohydr. Polym. 2014;111:230-5.
[18] Fu L-H, Li S-M, Bian J, Ma M-G, Long X-L, Zhang X-M, et al. Compare study cellulose/Mn_3O_4 composites using four types of alkalis by sonochemistry method. Carbohydr. Polym.. 2015;115:373-8.
[19] Zhu C, Han C-g, Saito G, Akiyama T. Facile synthesis of MnO/carbon composites by a single-step nitrate-cellulose combustion synthesis for Li ion battery anode. J. Alloys Compd. 2016;689:931-7.
[20] Phoohinkong W, Sukonket T. Preparation of Nanosized Manganese Oxide Particles via Solid-State Route Reaction. Key Eng. Mater. 2016;675-676:146-9.
[21] Sofla MRK, Brown RJ, Tsuzuki T, Rainey TJ. A comparison of cellulose nanocrystals and cellulose nanofibres extracted from bagasse using acid and ball milling methods. Adv. Nat. Sci.: Nanosci. Nanotechnol. 2016;7:035004.
[22] Lam NT, Chollakup R, Smitthipong W, Nimchua T, Sukyai P. Characterization of Cellulose Nanocrystals Extracted from Sugarcane Bagasse for Potential Biomedical Materials. Sugar Tech 2017;19:539-52.
[23] Yan J, Fan Z, Wei T, Qian W, Zhang M, Wei F. Fast and reversible surface redox reaction of graphene–MnO_2 composites as supercapacitor electrodes. Carbon 2010; 48:3825-33.
[24] Qi Z, Younis A, Chu D, Li S. A Facile and Template-Free One-Pot Synthesis of Mn_3O_4Nanostructures as Electrochemical Supercapacitors. Nano-Micro Lett. 2016; 8:165-73.
[25] Gilbert B, Frazer BH, Belz A, Conrad PG, Nealson KH, Haskel D, et al. Multiple Scattering Calculations of Bonding and X-ray Absorption Spectroscopy of Manganese Oxides. J. Phys. Chem. A 2003;107:2839-47.
[26] Farges F. Ab initio and experimental pre-edge investigations of the Mn K-edge XANES in oxide-type materials. Phys. Rev. B 2005;71:155109.
[27] Liu J, Liu J, Song W, Wang F, Song Y. The role of electronic interaction in the use of Ag and Mn_3O_4 hybrid nanocrystals covalently coupled with carbon as advanced oxygen reduction electrocatalysts. J. Mater. Chem. A 2014;2:17477-88.

[28] Chalmin E, Farges F, Brown GE. A pre-edge analysis of Mn K-edge XANES spectra to help determine the speciation of manganese in minerals and glasses. Contrib. Mineral. Petrol. 2009;157:111-26.
[29] Manceau A, Gorshkov AI, Drits V. Structural chemistry of Mn, Fe, Co, and Ni in manganese hydrous oxides; Part II, information from EXAFS spectroscopy and electron and X-ray diffraction. Am. Mineral. 1992;77:1144-57.
[30] Buciuman F, Patcas F, Craciun R, R. T. Zahn D. Vibrational spectroscopy of bulk and supported manganese oxides. Phys. Chem. Chem. Phys. 1999;1:185-90.
[31] Kirillov SA, Aleksandrova VS, Lisnycha TV, Dzanashvili DI, Khainakov SA, García JR, et al. Oxidation of synthetic hausmannite (Mn_3O_4) to manganite (MnOOH). J. Mol. Struct. 2009;928:89-94.
[32] Li F, Wu J, Qin Q, Li Z, Huang X. Facile synthesis of γ-MnOOH micro/nanorods and their conversion to β-MnO_2, Mn_3O_4. J. Alloys Compd. 2010;492:339-46.
[33] Zhang WX, Yang ZH, Liu Y, Tang SP, Han XZ, Chen M. Controlled synthesis of Mn_3O_4 nanocrystallites and MnOOH nanorods by a solvothermal method. J. Cryst. Growth 2004;263:394-9.
[34] Kohler T, Armbruster T, Libowitzky E. Hydrogen Bonding and Jahn–Teller Distortion in Groutite,α-MnOOH, and Manganite,γ-MnOOH, and Their Relations to the Manganese Dioxides Ramsdellite and Pyrolusite. J. Solid State Chem. 1997;133: 486-500.
[35] Kondo T, Sawatari C. A Fourier transform infra-red spectroscopic analysis of the character of hydrogen bonds in amorphous cellulose. Polymer 1996;37:393-9.
[36] Ren LZ, Zhou WQ, Wang YJ, Meng M, Wu SX, Li SW. Magnetic properties of Mn_3O_4 film with a coexistence of two preferential orientations. J. Appl. Phys. 2014;116:243-9.
[37] Wu KH, Zeng QC, Zhang BS, Leng X, Su DS, Gentle IR, et al. Structural Origin of the Activity in Mn_3O_4-Graphene Oxide Hybrid Electrocatalysts for the Oxygen Reduction Reaction. Chemsuschem 2015;8:3331-9.
[38] Zhang LS, Zhao LJ, Lian JS. Nanostructured Mn_3O_4-reduced graphene oxide hybrid and its applications for efficient catalytic decomposition of Orange II and high lithium storage capacity. RSC Adv. 2014;4:41838-47.
[39] Bose VC, Biju V. Mixed valence nanostructured Mn_3O_4 for supercapacitor applications. Bull. Mater. Sci. 2015;38:865-73.
[40] Liang X, Hart C, Pang Q, Garsuch A, Weiss T, Nazar LF. A highly efficient polysulfide mediator for lithium-sulfur batteries. Nat. Commun. 2015;6:6682.
[41] Quan B, Yu SH, Chung DY, Jin AH, Park JH, Sung YE, et al. Single Source Precursor-based Solvothermal Synthesis of Heteroatom-doped Graphene and Its Energy Storage and Conversion Applications. Sci. Rep. 2014;4:5639.
[42] Ganguly A, Sharma S, Papakonstantinou P, Hamilton J. Probing the Thermal Deoxygenation of Graphene Oxide Using High-Resolution In Situ X-ray-Based Spectroscopies. J. Phys. Chem. C 2011;115:17009-19.
[43] Ishizaki T, Wada Y, Chiba S, Kumagai S, Lee H, Serizawa A, et al. Effects of halogen doping on nanocarbon catalysts synthesized by a solution plasma process for the oxygen reduction reaction. Phys. Chem. Chem. Phys. 2016;18:21843-51.
[44] Wong CHA, Pumera M. Highly conductive graphene nanoribbons from the reduction of graphene oxide nanoribbons with lithium aluminium hydride. J. Mater. Chem. C 2014;2:856-63.
[45] Khiari R, Salon MCB, Mhenni MF, Mauret E, Belgacem MN. Synthesis and characterization of cellulose carbonate using greenchemistry: Surface modification of Avicel. Carbohydr. Polym. 2017;163:254-60.

[46] Peng X, Shen SG, Wang CY, Li TJ, Li YH, Yuan SJ, et al. Influence of relative proportions of cellulose and lignin on carbon-based solid acid for cellulose hydrolysis. Mol. Catal. 2017;442:133-9.
[47] Chavez-Guerrero L, Sepulveda-Guzman S, Silva-Mendoza J, Aguilar-Flores C, Perez-Camacho O. Eco-friendly isolation of cellulose nanoplatelets through oxidation under mild conditions. Carbohydr. Polym. 2018;181:642-9.
[48] Park S, Lee KS, Bozoklu G, Cai W, Nguyen ST, Ruoff' RS. Graphene oxide papers modified by divalent ions - Enhancing mechanical properties via chemical cross-linking. Acs Nano 2008;2:572-8.
[49] Tang MM, Bacon R. Carbonization of cellulose fibers—I. Low temperature pyrolysis. Carbon. 1964;2:211-20.
[50] Figueiredo JL, Pereira MFR, Freitas MMA, Órfão JJM. Modification of the surface chemistry of activated carbons. Carbon. 1999;37:1379-89.
[51] Song YZ, Zhao RX, Zhang KK, Ding JJ, Lv XM, Chen M, et al. Facile synthesis of Mn_3O_4/double-walled carbon nanotube nanocomposites and its excellent supercapacitive behavior. Electrochim. Acta 2017;230:350-7.
[52] Yang ZL, Lu DL, Zhao RR, Gao AM, Chen HY. Synthesis of a novel structured Mn_3O_4@C composite and its performance as anode for lithium ion battery. Mater. Lett. 2017;198:97-100.
[53] Gao T, Krumeich F, Nesper R, Fjellvag H, Norby P. Microstructures, Surface Properties, and Topotactic Transitions of Manganite Nanorods. Inorg. Chem. 2009;48:6242-50.
[54] Oh YJ, Yoo JJ, Kim YI, Yoon JK, Yoon HN, Kim JH, et al. Oxygen functional groups and electrochemical capacitive behavior of incompletely reduced graphene oxides as a thin-film electrode of supercapacitor. Electrochim. Acta 2014;116:118-28.
[55] Biesinger MC, Payne BP, Grosvenor AP, Lau LWM, Gerson AR, Smart RSC. Resolving surface chemical states in XPS analysis of first row transition metals, oxides and hydroxides: Cr, Mn, Fe, Co and Ni. Appl. Surf. Sci. Adv. 2011;257:2717-30.
[56] Wei WF, Cui XW, Chen WX, Ivey DG. Manganese oxide-based materials as electrochemical supercapacitor electrodes. Chem. Soc. Rev. 2011;40:1697-721.
[57] Ribeiro RAP, de Lazaro SR, Pianaro SA. Density Functional Theory applied to magnetic materials: Mn_3O_4 at different hybrid functionals. J. Magn. Magn. Mater. 2015;391: 166-71.
[58] Smith PF, Deibert BJ, Kaushik S, Gardner G, Hwang SJ, Wang H, et al. Coordination Geometry and Oxidation State Requirements of Corner-Sharing MnO_6 Octahedra for Water Oxidation Catalysis: An Investigation of Manganite (gamma-MnOOH). Acs Catal. 2016;6:2089-99.
[59] Nesbitt HW, Banerjee D. Interpretation of XPS Mn(*2p*) spectra of Mn oxyhydroxides and constraints on the mechanism of MnO_2 precipitation. Am. Mineral. 1998;83:305-15.
[60] Gupta RP, Sen SK. Calculation of multiplet structure of core p-vacancy levels. Phys. Rev. B 1974;10:71-7.
[61] Gupta RP, Sen SK. Calculation of multiplet structure of core p-vacancy levels. II. Phys. Rev. B 1975;12:15-9.
[62] Oku M, Hirokawa K, Ikeda S. X-ray photoelectron spectroscopy of manganese-oxygen systems. J. Electron. Spectrosc. Relat. Phenom. 1975;7:465-73.
[63] Oku M, Hirokawa K. X-ray photoelectron spectroscopy of Co_3O_4, Fe_3O_4, Mn_3O_4, and related compounds. J. Electron. Spectrosc. Relat. Phenom. 1976;8:475-81.
[64] Ilton ES, Post JE, Heaney PJ, Ling FT, Kerisit SN. XPS determination of Mn oxidation states in Mn (hydr)oxides. Appl. Surf. Sci. 2016;366:475-85.

[65] Grissa R, Martinez H, Cotte S, Galipaud J, Pecquenard B, Le Cras F. Thorough XPS analyses on overlithiated manganese spinel cycled around the 3V plateau. Appl. Surf. Sci. 2017;411:449-56.
[66] Oku M. X-ray photoelectron spectra of $KMnO_4$ and K_2MnO_4 fractured in situ. J. Electron. Spectrosc. Relat. Phenom. 1995;74:135-48.
[67] Xia XH, Lu L, Walton AS, Ward M, Han XP, Brydson R, et al. Origin of significant visible-light absorption properties of Mn-doped TiO2 thin films. Acta Mater. 2012;60:1974-85.
[68] Aghazadeh M, Maragheh MG, Ganjali MR, Norouzi P. One-step electrochemical preparation and characterization of nanostructured hydrohausmannite as electrode material for supercapacitors. RSC Adv. 2016;6:10442-9.